CREATIVE SCIENCE

Journal home page: csj.snru.ac.th



Impact of alkaline salts loading on structural, optical and Near-infrared shielding properties of potassium tungsten bronze materials

Phonlawee Pinthong [a*], Maneerat Songpanit [a], Thanaphon Kansaard [a], Wanichaya Mekprasart [a], Kanokthip Boonyarattanakalin [a] and Wisanu Pecharapa [a]

[a] *Department of Nanoscience and Nanotechnology, School of Integrated Innovative Technology (SIITec), King Mongkut's Institute of Technology Ladkrabang, Bangkok, 10520, Thailand*

Article history:

Received: 06-02-2026
Revised : 23-03-2026
Accepted: 07-04-2026
Published: 02-06-2026

Keywords:

Potassium tungsten bronze;
Ball milling process;
Near-infrared shielding.

Abstract

Increasing heat emissions through windows directly affect energy consumption in air conditioner systems. To address this challenge, potassium tungsten bronze (K_xWO_3) materials are used for near-infrared shielding. The materials provide high transmission in the visible region and strong absorption at infrared wavelengths. The optical properties of these materials depend on the ratio of alkali metal to tungsten, which determines the number of donor electrons available from the alkali metal, and also the extent of reduction of tungsten from its W^{6+} oxidation state to its W^{5+} state. This interplay between oxidation states gives rise to the phenomena of localized surface plasmon resonance (LSPR) and small polaron absorption. In this work, we investigated various values of x in K_xWO_3 where x = 0.1, 0.3, 0.5, and 0.7, using a high-energy ball milling method to synthesize the K_xWO_3 powders. Characterization was conducted using X-ray diffraction (XRD) for crystalline structure, field emission scanning electron microscopy (FESEM) for powder morphology determination, X-ray photoelectron spectroscopy (XPS) for the study of the oxidation states of tungsten (W), and ultraviolet–visible–near-infrared) spectroscopy (UV–vis–NIR) for optical property investigation. The results provide correlations between the potassium ratio, the crystal structure, and the NIR shielding performance of potassium tungsten bronze materials.

*** Corresponding author** : 67116004@kmitl.ac.th

DOI: https://doi.org/10.55674/cs.v18i3.266086

© [2026] The Author(s).

1. Introduction

Solar radiation provides light and also heats. The increasing severity of global warming directly impacts energy consumption and indoor comfort [1, 2]. Almost 40% of energy consumption is used in HVAC systems (heating, ventilation, and air conditioning). To solve this issue, thermal insulation technologies such as radiant barriers, cool paints, and low-emission glass materials are currently under ongoing research and development. However, the loss of energy is mainly caused by radiative transfer across glass windows [3]. In particular, infrared wavelengths pass through conventional glass and get converted into heat, causing the internal building temperature to rise. Various types of materials with high transparency to visible light and low near-infrared transmission have been explored to decrease near-infrared radiation. On one hand, the addition of a shading system, such as a façade can be used to prevent heat emission into buildings [4] .

On the other hand, transparent insulation coating materials on glass windows have been used effectively to solve this problem. Materials that have been studied, such as antimony-doped tin oxide (ATO) [5 - 7], indium-doped tin oxide (ITO) [8], and lanthanum hexaboride (LaB_6) [9] , have shown promising infrared shielding potential. However, they are of limited value due to their low near-infrared absorption ability and their high cost of complex preparation. Tungsten oxide materials (WO_3) which commonly known as n-type semiconductor materials with band gap around 3.0 eV. tend to be an interesting alternative, with better coverage in the near-infrared absorption region and a non-complicated preparation process. Tungsten oxide materials consist of networks of tungsten octahedra (WO_6) in which tungsten (W) atoms occupy the body center and oxygen atoms (O) occupy the corners. To improve near-infrared absorption efficiency, alkali metals such as lithium (Li) [10], sodium (Na) [11 - 13], potassium (K) [14 - 16], rubidium (Rb) [17], and cesium (Cs) [18 - 21] are added to form M_xWO_3 compounds, which are collectively known as tungsten bronze materials (M_xWO_3, x=0.33). These materials have three main structures: cubic, tetragonal, and hexagonal [9, 22] . The cubic and tetragonal structures have smaller void spaces radius approximately 1.43 Å, allowing Li^+ and Na^+ to be inserted with x-values between 0.5 and 1. The hexagonal structures have wider void spaces of approximately 1.63 Å, allowing larger atoms such as K^+ (1.38 Å) and Cs^+ (1.67 Å) to be inserted with x-values between 0.2 and 0.33 [22, 23]. The

hexagonal structure Cesium tungsten bronze exhibits superior shielding performance. However, due to limitations in cost-effectiveness and large-scale applications, potassium tungsten bronze (K_xWO_3) is attracting more research interest due to its stable hexagonal structure and optimal ion size of potassium that make it suitable for near-infrared shielding applications.

Tungsten bronze materials are mainly synthesized via wet-chemical processes such as the hydrothermal [24 - 26] and solvothermal methods [27 - 30]. On a laboratory scale, these two methods are effective for controlling morphology, structure, and size. However, they involve long synthesis times. Although solid-state synthesis requires a shorter reaction time than hydrothermal and solvothermal methods, it necessitates significantly higher temperatures [31 - 33] .The mechanochemical method is another compromise that is environmentally friendly. While this method is typically used to reduce particle size or homogenize powders, it was, in this work, applied to induce chemical reactions via the impact forces between the milling balls and particles. Wang *et al.* [18] successfully prepared cesium tungsten bronze ($Cs_{0.32}WO_3$) nanoparticles using the high-energy ball milling method. The addition of cellulose as a reducing agent promoted the formation of pentavalent tungsten (W^{5+}), which exhibited near-infrared shielding ability. The addition of alkali metals increases electron concentration in tungsten bronze (M_xWO_3) materials and results in near-infrared radiation shielding. This occurrence can be explained by two phenomena localized surface plasmon resonance (LSPR) and small polaron absorption [34 - 35].

In this work, we aim to study the impact on the structural, optical, and near-infrared shielding performance of potassium tungsten bronze (K_xWO_3) with different potassium loading ratios (x = K/W) at x = 0.1, 0.3, 0.5 and 0.7, using a high-energy ball milling process. The characterization was conducted using several techniques to confirm the near-infrared shielding performance of the potassium tungsten bronze materials.

2. Materials and Methods

Materials

To synthesize K_xWO_3 materials, potassium chloride (KCl) (99%, KemAus Co.) was used as the potassium source, along with tungstic acid (H_2WO_4) and cellulose ($(C_6H_{10}O_5)_n$). For film preparation, polyvinyl alcohol (PVA, $[CH_2CH(OH)]_n$) was used as a film binder and was purchased from Sigma Aldrich Co. All chemicals were used as starting materials without further purification.

Synthesis of x-KWO particles

Potassium tungsten bronze materials were synthesized by the high energy ball milling method. H_2WO_4, KCl and cellulose were placed into a milling jar. The different ratios of potassium and tungsten (K/W) in the potassium tungsten bronze (K_xWO_3) were for x= K/W at 0.1, 0.3, 0.5, and 0.7 respectively. The homogenization process involved an initial ball-to-powder ratio of 10:1, followed by a drying process. The powders were milled again with increased ratio of 20 to 1. To produce more impact force inside, the milling times were set to 6 hours. Finally, the powders were dried at 80°C overnight and named as 0.1 0.3, 0.5 and 0.7-KWO respectively.

Film coating preparation

The as-prepared x-KWO powder sample was dispersed in deionized water under stirring for 30 min. Concurrently, polyvinyl alcohol, which was used as film binder, was dissolved at a concentration 10%wt with deionized water. After that, 0.1 g of each dispersed x-KWO powder was added into the PVA solution and stirred for 24 hours to obtain a homogenous film slurry. Each slurry was coated onto a glass pane using the simple doctor blade method, and dried at 80 °C in the oven overnight.

Materials characterization

With respect to the instruments used for analysis, an x-ray diffractometer was employed to study the crystal structure of the prepared-powder samples. The instrument was equipped with a Cu-Kα x-ray source (wavelength 1.54 Angstrom), and measurement was conducted in the theta-2-theta mode from 10° to 80° with scan rate velocity at 10° per min. The morphology and elemental composition of each KWO powder at different K/W loadings were analyzed with a field-emission electron microscope combined with energy dispersive spectroscopy (FE-SEM, JOEL, JSM-7001F). Furthermore, for more advanced surface analysis, an x-ray photoelectron spectrometer (XPS, ULVAC-PHI, VersaProbe-4) was utilized to determine oxidation states. In addition, to further investigate optical properties, the transmission of the x-KWO films in the wavelength range of 240-2500 nm was measured using a UV-Vis-NIR spectrometer (UV-VIS, HITACHI, UH-1450, Japan). While the film thickness was evaluated by stylus profilometer (stylus profiler, Bruker, Dektak XT) the measurement were conducted with 3.5 mg of stylus force at scan speed of 10 μm s^{-1}. To establish the near-infrared shielding performance, a heat insulation test system was constructed for the validation and was combined with an infrared lamp (Philips, BR125 IR 250W), which served as a heating source.

3. Result and discussion

Crystal structure

The XRD analysis showed the diffraction patterns of potassium tungsten bronze (x-KWO) powder at the loading ratios of 0.1, 0.3, 0.5, and 0.7. The results can be seen in Fig. 1. At the low loading ratio of 0.1 (0.1 KWO), the diffraction pattern was similar to that of tungsten oxide (WO_3, JCPDS No.00-085-2459). At the 0.3 KWO condition, the diffraction peaks became sharp, which indicated better crystallinity as shown in Table 1. The diffraction peaks at 2θ° from 55° to 62° indicated the (2 2 2), (2 0 4) and (4 0 0) planes typical of the hexagonal structure of potassium tungsten bronze ($K_{0.33}WO_3$, JCPDS No.00-026-1340). This was likely indicative of potassium ions having been inserted into hexagonal interstitial spaces forming potassium tungsten bronze (h-K_xWO_3).

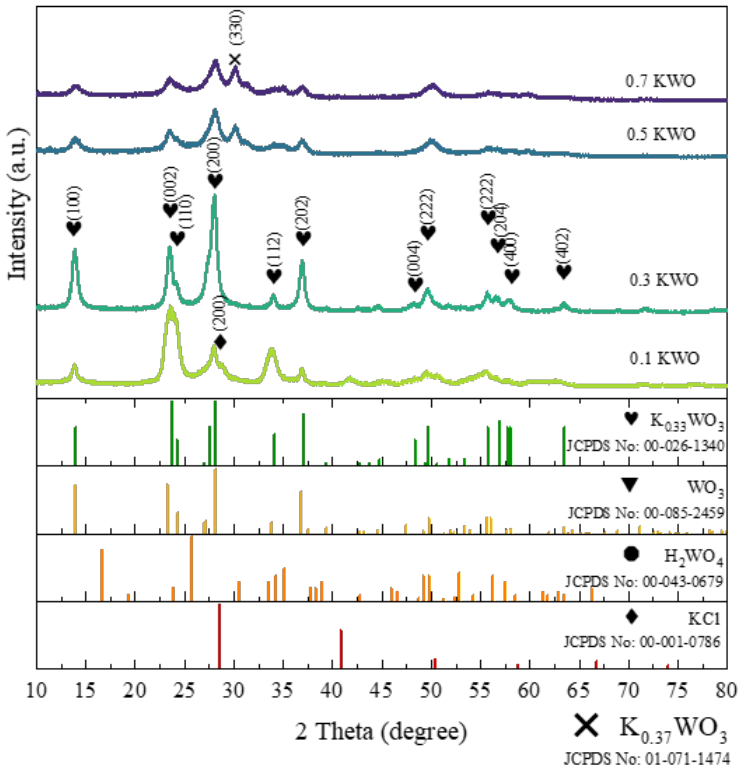


Fig. 1 XRD patterns of x-KWO at difference K/W loadings at x=0.1, 0.3, 0.5 and 0.7 respectively.

Table 1 d-spacing and lattice parameters.

Samples	d-spacing (200) (Å)	Average Crystallite size (nm)	Lattice parameter (Å)	
			a = b	c
0.1-KWO	3.18	76.40	3.90	7.62
0.3-KWO	3.19	106.35	3.90	7.56
0.5-KWO	3.16	54.96	3.88	7.61
0.7-KWO	3.16	48.66	3.88	7.52

However, with higher loading ratios of potassium at 0.5 and 0.7, the intensity of the already mentioned peaks decreased and new peaks arose at 2θ° diffraction angles around 30°, which corresponded to the (3 3 0) plane of $K_{0.37}WO_3$ (JCPDS No.01-071-1474) and indicated tetragonal structure. As indicated in earlier work on IR shielding applications, the optimal phase structure is the hexagonal one [12, 14], and the existence of other structures adversely affect near-infrared shielding.

Morphology and Elemental composition

The morphology and microstructure of the potassium tungsten bronze synthesized with the varied different potassium loading ratios of 0.1, 0.3, 0.5 and 0.7 were analyzed by field-emission scanning electron microscopy, and the results are shown in Fig. 2(a-d). At the 0.1 and 0.3 conditions, particles size approximately 300-355 nm can be seen. But at the higher potassium loading ratios in 0.5-KWO and 0.7-KWO conditions, the samples showed an uneven size distribution, which revealed that the small particles–found may have come from the formation of another phase, which would be in agreement with the diffraction patterns in Fig. 1.

The elemental composition of the potassium tungsten bronze with different potassium loading ratios was confirmed by energy-dispersive-spectroscopy (EDS) mapping and the results can be seen Fig. 2 (e-h), which shows the presence of potassium, tungsten, and oxygen, and confirmed that these elements were uniformly distributed by the high energy ball milling process. The EDS also showed the atomic ratio between potassium (K) and tungsten (W) in the powder samples, as can be seen in Table 2.

The EDS results showed that at the 0.1-KWO condition, the measured ratio was only 0.06, indicating that potassium atoms were not completely incorporated into the hexagonal tunnel space. This correlated with the X-ray diffraction results above that showed the presence of a mixed phase of tungsten oxide (WO_3) and potassium tungsten bronze (K_xWO_3). At the 0.3-KWO condition, the measured atomic ratio was 0.21, which was closer to the ideal ratio of around 0.33 ($K_{0.33}WO_3$).

Table 2 EDS analysis of x-KWO at difference K/W loadings at x=0.1, 0.3, 0.5 and 0.7 respectively.

Sample	Average Size distribution (nm)	Atomic (%)			K/W
		K	W	O	
0.1-KWO	354.7	0.80	12.22	86.91	0.06
0.3-KWO	319.0	3.45	16.17	80.09	0.21
0.5-KWO	305.7	2.24	13.52	83.93	0.17
0.7-KWO	338.5	1.87	10.47	87.66	0.18

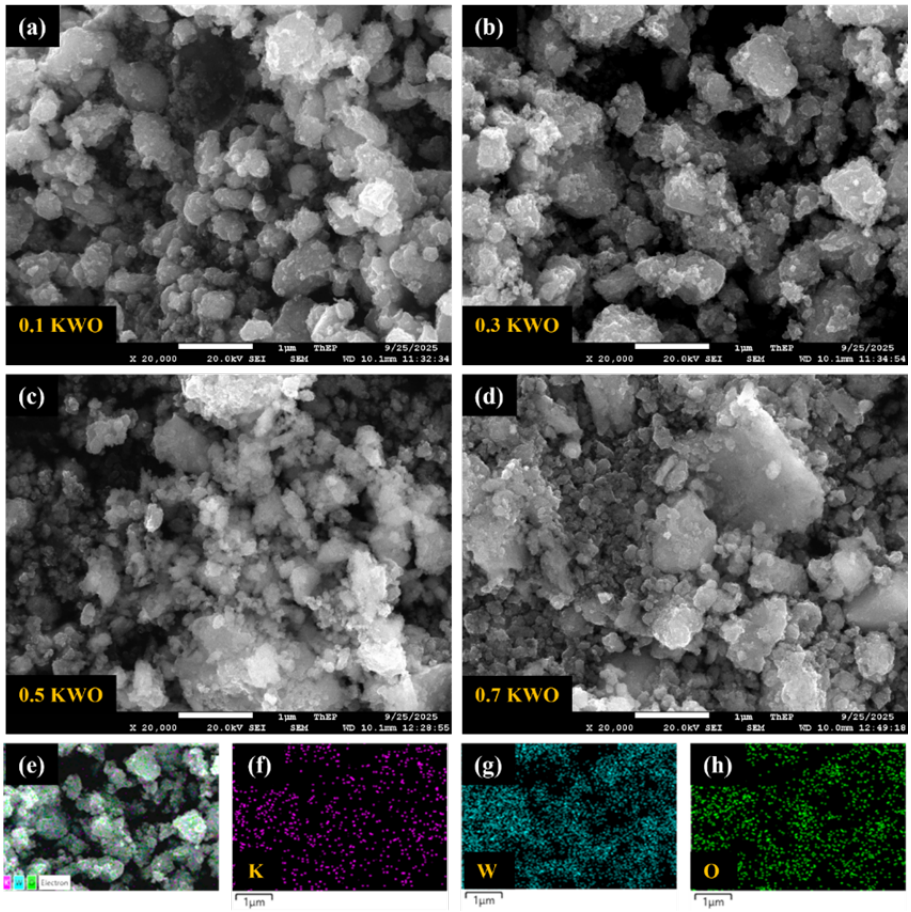


Fig. 2 (a-d) FESEM micrographs of x-KWO at difference K/W loadings (x = 0.1, 0.3, 0.5 and 0.7) and (e-h) EDS mapping of 0.3-KWO powder sample.

This shows that most of interstitial space was filled with potassium atoms. However, at higher potassium loading ratios, that is for the 0.5-KWO and 0.7-KWO samples, the measured ratios decreased markedly to around 0.17 and 0.18 respectively. This was likely due to potassium being loaded into the hexagonal structure at a level beyond its stoichiometric limit of around 0.33 . The resultant excess potassium ions formed a mixed tetragonal phase external to the hexagonal structure that was removed during chloride washing. This resulted in the final atomic ratio being lower than expected.

In order to verify elemental composition, X-ray photoelectron spectroscopy (XPS) was conducted in the survey scan mode, and the results are presented in Fig. 3 (a–d). For the 0.3-KWO sample, the survey spectrum confirmed the presence of tungsten (W), oxygen (O), and potassium (K), with potassium signals observed in the binding energy range of 290–298 eV. In contrast, the survey spectrum of pristine tungsten oxide (WO_3) revealed only tungsten (W) and oxygen (O), with no detectable potassium or other impurities, as shown in Fig. 3(a).

To clarify near-infrared shielding properties of the potassium tungsten bronze, deconvoluted XPS spectra were employed to analyze the oxidation states of the elements present. The oxidation state of tungsten (W) was used to indicate near-infrared shielding due to the small polaron phenomena, as can be seen in Fig 3(c).

The W^{4f} core-level deconvoluted spectra at binding energy of around 31.0 - 41.0 eV displayed a spin orbit doublet, with peaks corresponding to the $W^{4f}{}_{5/2}$ and $W^{4f}{}_{7/2}$ states. The stable oxidation state of tungsten in the W4f core-level spectra is typically the hexavalent W^{6+} state. As shown in Fig 3(c), the

peaks at lower binding energies corresponded to the pentavalent tungsten W^{5+} state. The presence of the W^{5+} oxidation state suggests that some of the W^{6+} ions had been reduced to W^{5+} to maintain charge balance in the structure with increasing amount of potassium (K^{+}) loading.

In Fig. 3(d) and 3(f), the oxidation state of oxygen at the O1s core level (around 528-536 eV) indicates lattice oxygen (Olattice, W-O) and oxygen vacancies (O vacancy). The oxygen vacancies act as electron donors, reducing the oxidation state of tungsten ions from W^{6+} to W^{5+}. This electronic state triggers localized surface plasmon resonance (LSPR) and small polaron absorption, resulting in near-infrared shielding properties while maintaining high transparency in the visible light region [31].

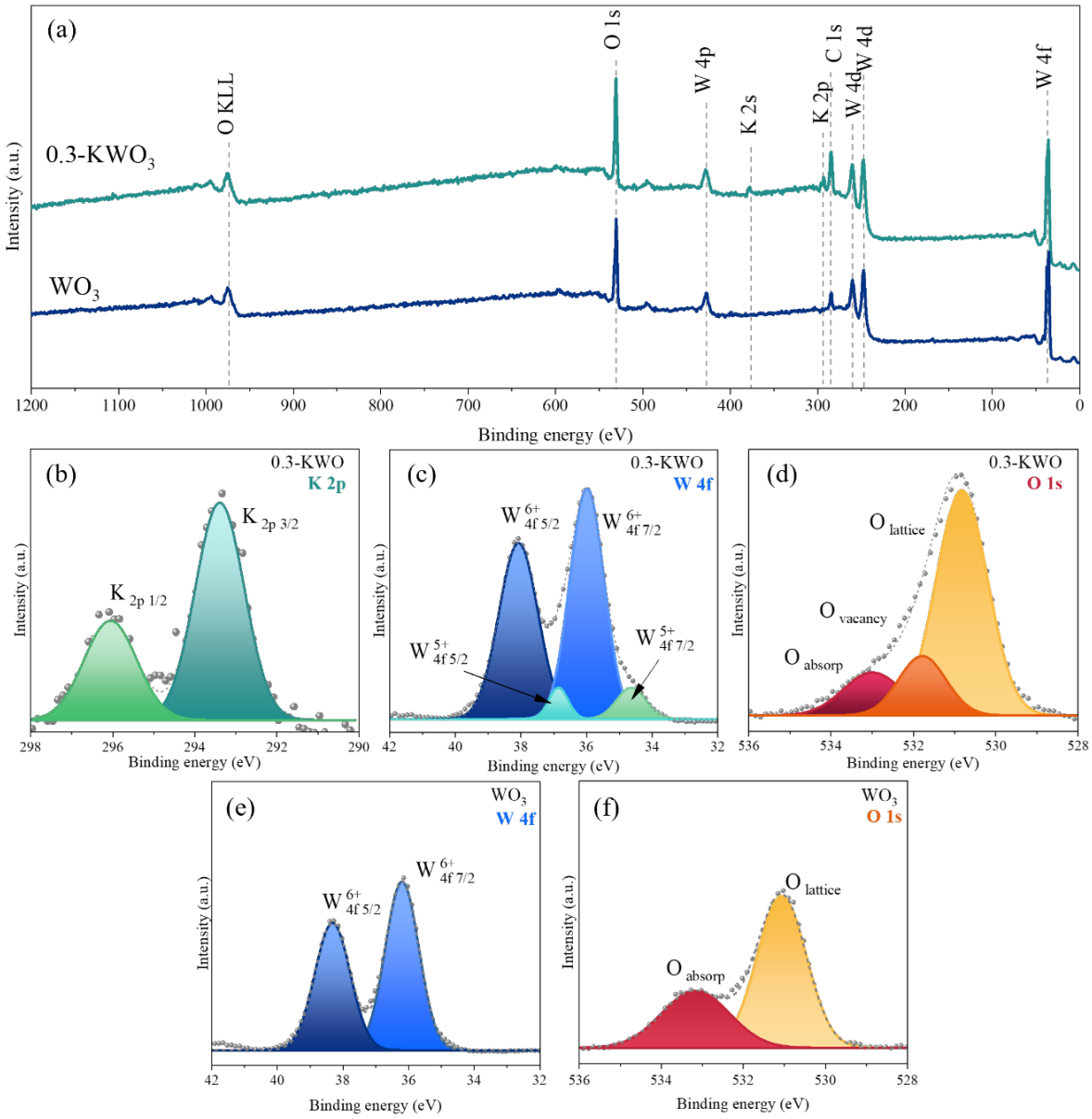


Fig. 3 XPS spectra of (a) survey scan, (b-d) deconvoluted spectrum at core-level of K 2p, W 4f and O 1s under the 0.3-KWO condition and (e-f) deconvoluted spectrum at W4f and O 1 score-level in WO_3.

Optical properties

The optical bandgap of synthesized potassium tungsten bronze powder with difference K loading ratio was determined as shown in Fig.4 and summarized in Table 3. The energy band gap (Eg) of pure WO_3 were around 3.3 eV, for 0.1-KWO and 0.3-KWO condition, Eg were found to be 2.91 and 2.96 eV respectively. Which show the carrier injection from K^{+} into WO_3 structure and, but higher loading ratio at 0.5-KWO and 0.7-KWO condition were show Eg at 3.44 and 3.49 eV, which more than WO3. The result related with EDS result that show lower atomic ratio of K/W, which indicate K^{+} are incomplete interstitial space when higher loading ratio. After film preparation, the optical properties of potassium tungsten bronze materials were examined for near-infrared

shielding applications at the potassium loading ratios of 0.1, 0.3, 0.5, and 0.7. The x-KWO powders were coated on glass panes with polyvinyl alcohol as the film binder. The thickness of film sample was measure by stylus profiler technique. For PVA coating sample without x-KWO content, the thickness of 6.28 ± 0.99 µm. Upon the potassium tungsten bronze powder addition, the thickness was around 6.03-9.52 µm, as summarized in Table 3.

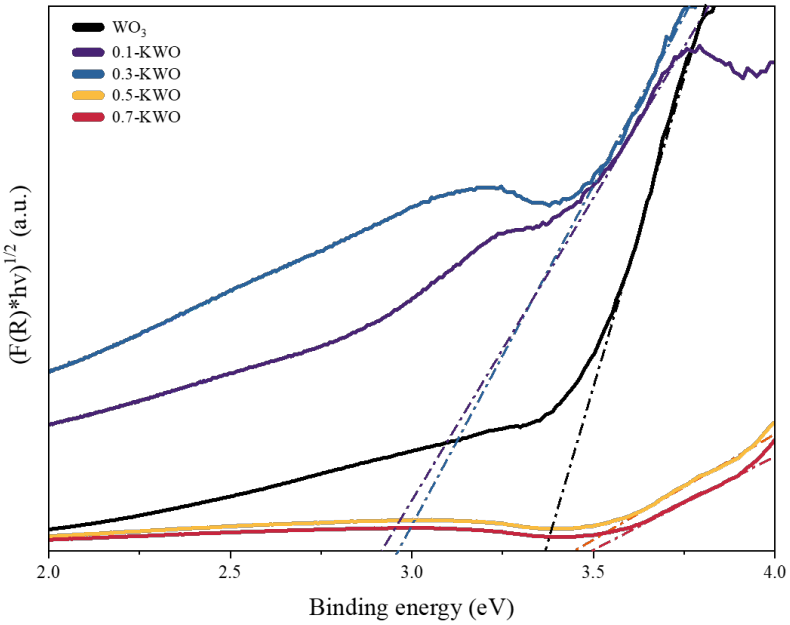


Fig. 4 Tauc plot of KWO powder with different K/W ratio loadings with x = 0.1, 0.3, 0.5 and 0.7.

Table 3 Film thickness and powder optical band gap of x-KWO samples.

Samples	Film Thickness (µm)	Eg (eV)
WO_3	-	3.36
PVA	6.28 ± 0.99	-
0.1 KWO	9.52 ± 0.81	2.91
0.3 KWO	6.92 ± 0.45	2.96
0.5 KWO	7.18 ± 1.36	3.44
0.7 KWO	6.03 ± 0.10	3.49

The composition was measured by XRD with film mode, as shown in Fig 5. The diffraction pattern of x-KWO were correlated with potassium tungsten bronze powder sample in Fig. 1, which shown characteristic peak of K0.33WO3 (JCPDS no.00-026-1340). After preparation to film coating slurry with PVA binder, the diffraction pattern was observed with new diffraction peak around 19.2° which related to PVA (JCPDS no.00-053-1847), as shown in Fig. 5.

To ensure the infrared shielding, all of x-KWO film samples were measured for transmittance across the visible to infrared region (380-2500 nm) as shown in Fig. 6(a-d). All samples were compared with normal glass panes and glass coated with film binder only. The obtained potassium tungsten bronze films demonstrated near-infrared shielding ability with more than 70% transparency in visible region while effectively suppressing transmission in the 780-1500 nm range. Among these samples, the 0.3-KWO sample exhibited the highest transparency while demonstrating a near-infrared shielding performance (Δ(%T) of 7.5%, which was the highest among the variants effectively suppressing transmission in the 780-1500 nm range. Among these samples, the 0.3-KWO sample exhibited the highest transparency while demonstrating a near-infrared shielding performance (Δ(%T) of 7.5%, which was the highest among the variants.

Moreover, higher photon energy enhanced the near-infrared shielding ability by promoting free carriers in WO6 lattice. This process led to the creation of large numbers of tungsten-pentavalent ions (W^{5+}), which in turn strengthened NIR absorption via the combined phenomena of small polaron transitions and localized surface plasmon resonance. An Ultraviolet (UVC) lamp was employed to simulate the ultraviolet component of solar radiation. After the films were exposed and measured for transmission, the films showed better absorption in the near-infrared region compared to samples without UV exposure, which was consistent with the combination of small polaron transitions and localized surface plasmon resonance.

Furthermore, longer exposure time resulted in stronger near-infrared absorption performance, especially in the 0.3-

KWO sample, which exhibited up to 54.7% near-infrared shielding at around 1250 nm. It also showed the highest Δ(%T) at 25.3% transparent insulation index (K), indicating high transparency and at the same time good IR shielding ability compared to the other samples, as can be seen in Table 4.

Near-Infrared shielding performance

In order to confirm effectiveness of the near-infrared shielding performance, a model test-box (20 cm×20 cm×30 cm) was constructed and used to examine the thermal shielding of the x-KWO film samples. The test-box was made from polystyrene foam and covered with aluminum foil as an insulation layer. The x-KWO film samples (5cm × 5cm) were placed on top of the test box. An infrared light was employed as a heat source, and directed onto the film surface as shown in the schematic in Fig. 7(a).

When K^+ enters the tunnel structure, free electrons are perturbed by electromagnetic wavelengths. The electrons then resonate at their natural frequency. Furthermore, free electrons are located in the conduction band and cause lattice distortion in WO_6, leading to a small polaron transition between W^{6+} and W^{5+}. This is shown in Equation (1), where A and B label different sites of tungsten (W), and *hv* and E_{phonon} refer to photon energy and phonon energy, respectively.

$$hv + W^{6+}_{(A)} + W^{5+}_{(B)} \rightarrow W^{5+}_{(A)} + W^{6+}_{(B)} + E_{phonon} \quad (1)$$

As can be seen in Fig 7(b), after testing with 60 minutes of infrared exposure, the temperature within the test box progressively increased. The recorded internal temperature in the case of the blank glass reached 37.7°C, whereas the potassium tungsten bronze film samples exhibited lower internal temperatures. Specifically, the optimal condition was 0.3-KWO, which produced an internal temperature that was lower than that of glass by 3.2°C.

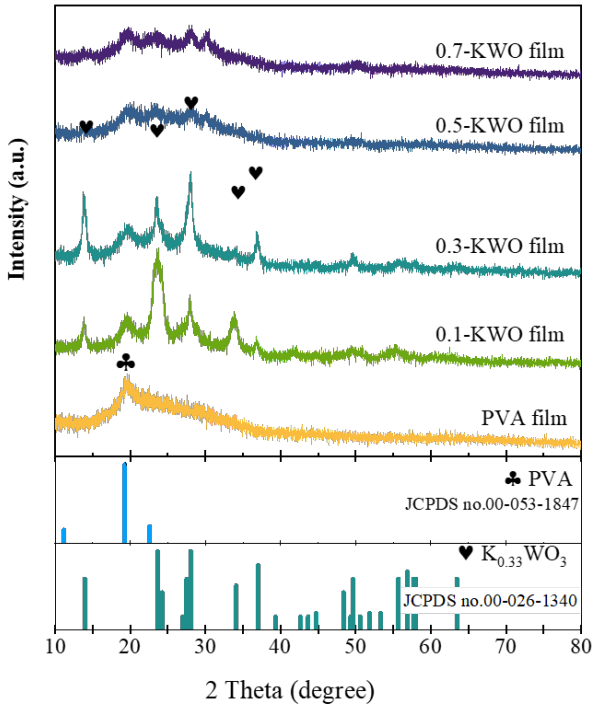


Fig. 5 XRD pattern of x-KWO film with different K/W loadings with x=0.1, 0.3, 0.5 and 0.7.

Table 4 Optical performance of x-KWO films

Sample	$\%T_{vis}$ max	$\%T_{NIR}$ min	Δ%T (vis-NIR)	$K=\frac{T_{vis}}{T_{NIR}}$
0.1 KWO	68.8	65.5	3.3	1.05
0.1 KWO- UV 90	67.1	48.4	18.7	1.39
0.3 KWO	*73.5*	*66.0*	*7.5*	*1.11*
0.3 KWO- UV 90	*70.7*	*45.3*	*25.3*	*1.56*
0.5 KWO	72.6	70.3	2.3	1.03
0.5 KWO- UV 90	71.9	64.5	7.4	1.11
0.7 KWO	68.9	67.0	1.9	1.03
0.7 KWO- UV 90	67.4	62.4	5.0	1.08

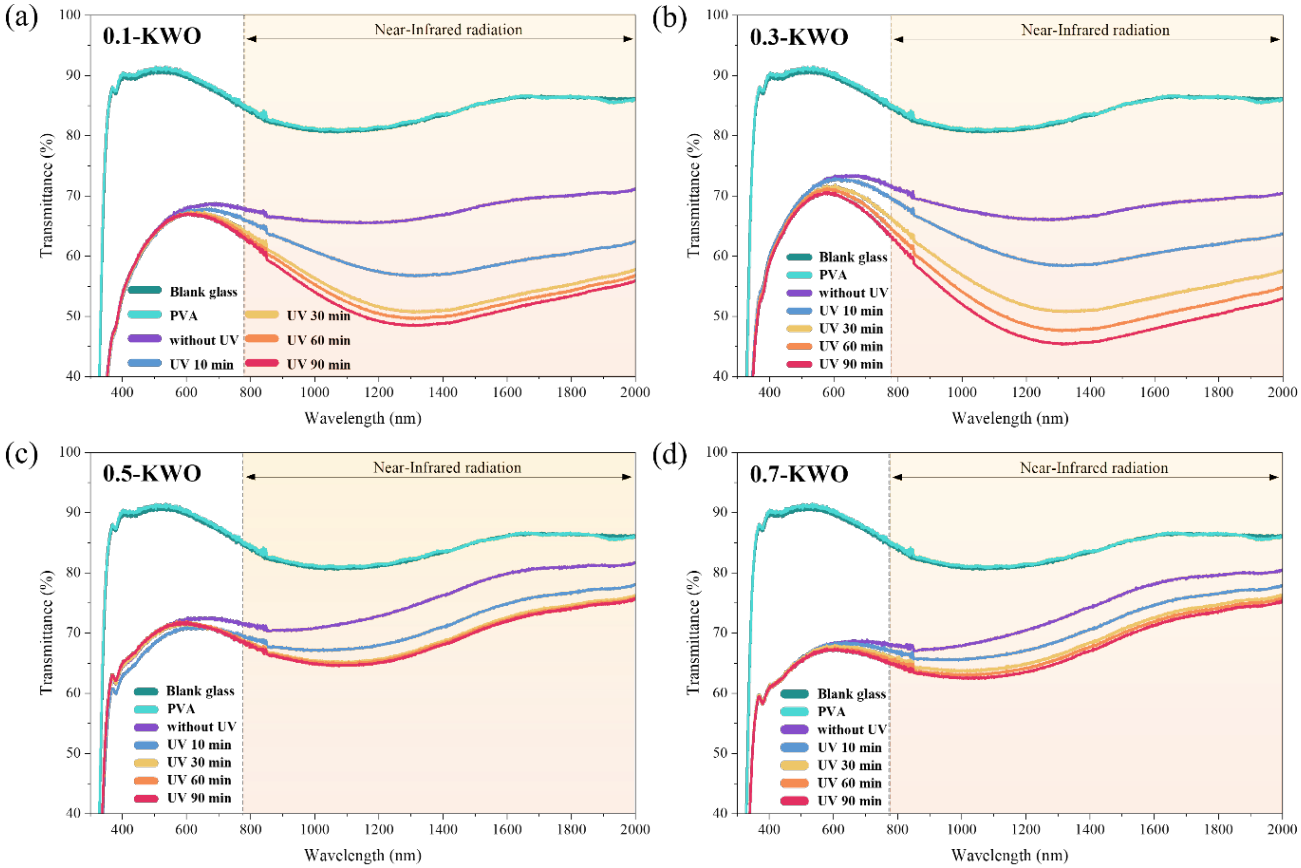


Fig. 6 Transmittance spectra of x-KWO at different K/W loadings with x=0.1, 0.3, 0.5 and 0.7 under difference UV radiation time at 10, 30, 60 and 90 min respectively.

This result was in agreement with the optical results. In addition, the combination of infrared and ultraviolet light sources showed stronger thermal shielding performance, as is seen in Fig.6(c). The higher photon energy promoted W^{5+} generation and small polaron transitions, which led to better near infrared absorption. The optical results (Fig. 6(a-d)) confirmed that the experimental films exhibited thermal shielding characteristics. All samples showed a lower internal temperature than did blank glass, as can be seen in Fig.7(c). This was especially true for the 0.3-KWO condition, for which the internal temperature measured was only 33.1°C, which was 4.6°C lower than that of the blank glass.

4. Conclusion

In summary, potassium tungsten bronze (K_xWO_3) samples of various potassium loading ratios (x) were successfully prepared by the high energy ball milling method. The results revealed that potassium loading had a significant influence on the crystal structure, optical properties, and thermal shielding performance of the x-KWO materials. At low loading concentration (0.1 and 0.3), predominantly hexagonal structures were observed, while at higher potassium loading, tetragonal structures were in greater number, leading to decreased shielding efficiency. XPS results confirmed that potassium- induced free electron production was taking place and that the liberated electrons reduced from W6+ to W5+. Moreover, these oxidation state transitions facilitated small polaron and localized surface plasmon resonance. The optical measurements demonstrated that the 0.3-KWO condition offered the highest visible light transmission (70.7-73.5 %) and effective near-infrared shielding performance. Furthermore, the materials exhibited better efficiency with UV exposure, with enhanced near-infrared shielding of up to 54.7% observed. Thermal insulation testing confirmed that the 0.3-KWO film reduced the internal temperature by 4.6°C compared to blank glass. Therefore, potassium tungsten bronze materials were promising candidates for smart window applications.

5. Acknowledgement

This work was supported by King Mongkut's Institute of Technology Ladkrabang (KMITL). The authors would like to thank the Nanocomposite Materials Research Laboratory (NMRL) participants, Advanced Technology Testing and Analysis Center (ATTAC), Department of Nanoscience and Nanotechnology and Advanced Engineering materials (AEM), School of Integrated Innovation Technology (SIITec) for providing characterization facilities.

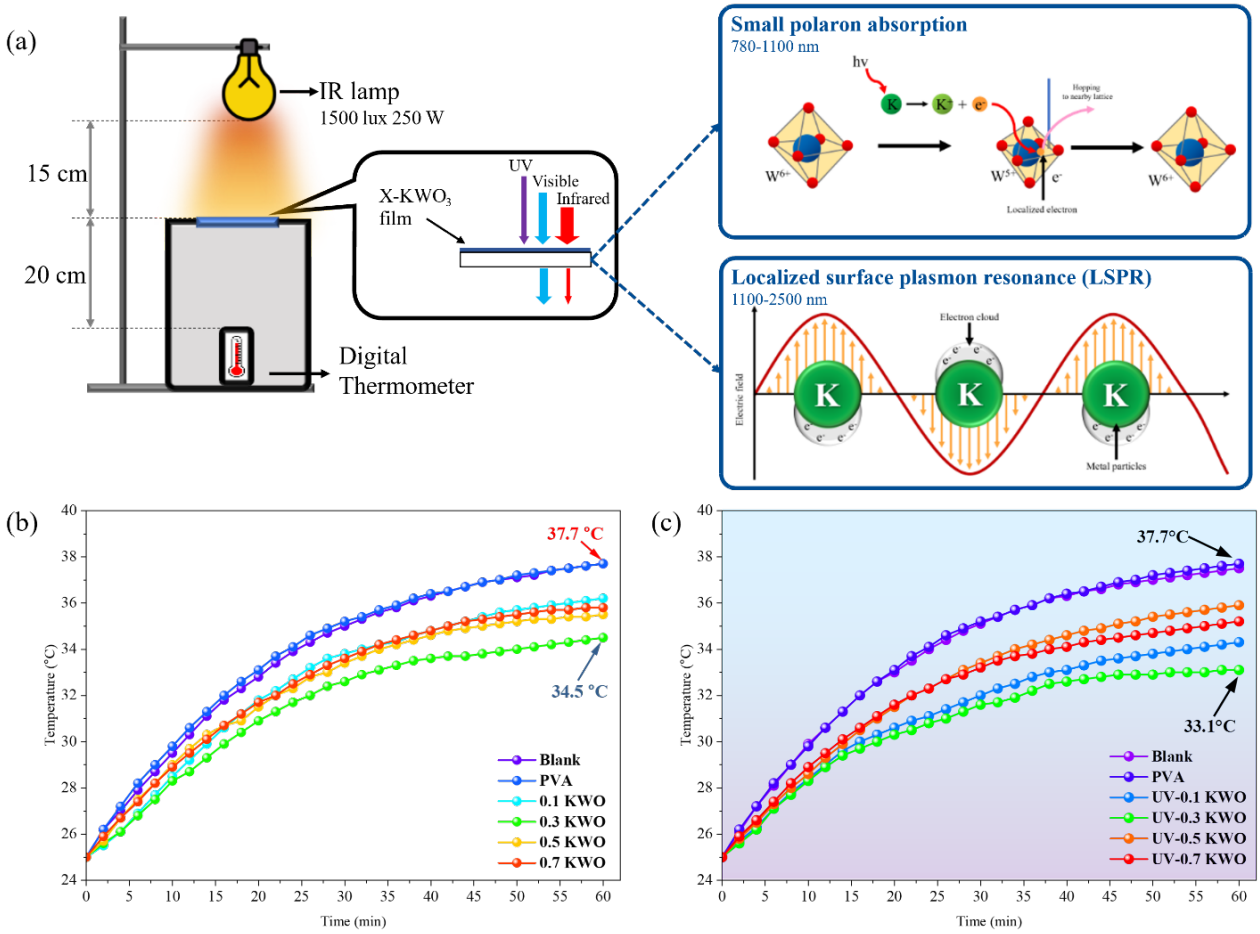


Fig. 7 (a) Schematic of near-Infrared shielding test, (b) Internal temperature with x-KWO film samples, and c) Internal temperature with x-KWO film samples with ultraviolet radiation

6. Declaration of Generative AI in Scientific Writing

The authors acknowledge the use of AI solely for grammatical error correction and language polishing. The scientific content, data analysis, and conclusions remain exclusively the work of the authors.

7. CRediT Author Statement

Phonlawee Pinthong: Writing – original draft, Methodology, Data curation. **Maneerat Songpanit:** Investigation, Validation. **Thanaphon Kansaard**: Investigation, Validation. **Wanichaya Mekprasart:** Writing – review & editing, Formal analysis. **Kanokthip Boonyarattanakalin:** Writing – review & editing, Formal analysis. **Wisanu Pecharapa:** Writing – review & editing, Supervision, Project administration.

8. Research Involving Human and Animals Right

Not applicable.

9. Ethics Approval and Consent to Participate

Not applicable.

10. Declaration of Competing Interest

The authors declare no competing interests.

11. References

[1] Arif, R., Tabrej, M. Q., Equbal, A., Equbal, M. A., Badruddin, I. A., Mahmoud, E. R. I., & Zuber, M. (2025). Multi-objective optimization approaches for enhancing building energy efficiency through material and equipment selection. *Case Studies in Thermal Engineering*, *75*, 107209. https://doi.org/10.1016/j.csite.2025.107209

[2] Bakhshi, M. H., Eftekhari Yekta, B., Rezaie, H., & Ashjari, A. (2024). Synthesis of transparent tin-doped indium oxide (ITO)-containing glass-ceramic coating by the sol-gel route for UV/NIR-shielding. *Optical Materials*, *153*, 115568. https://doi.org/10.1016/j.optmat.2024.115568

[3] Cai, Q., Li, X., Wen, L., Du, Y., Shi, Y., Sun, Y., Ding, B., Wang, Y., & Wang, S. (2024). In-situ growth of $Cs_{0.33}WO_3$@ATO composite material with enhanced NIR shielding rate for energy-saving coating. *Ceramics International*, *50*(19), 36691-36702. https://doi.org/10.1016/j.ceramint.2024.07.056

[4] Chao, L., Bao, L., Wei, W., & Tegus, O. (2019). A review of recent advances in synthesis, characterization and NIR shielding property of nanocrystalline rare-earth hexaborides

and tungsten bronzes. *Solar Energy*, *190*, 10-27. https://doi.org/10.1016/j.solener.2019.07.087

[5] Guo, C., Yin, S., Huang, L., & Sato, T. (2011). Synthesis of one-dimensional potassium tungsten bronze with excellent near-infrared absorption property. *ACS Appl Mater Interfaces*, *3*(7), 2794-2799. https://doi.org/10.1021/am200631e

[6] Gupta, V., & Deb, C. (2023). Envelope design for low-energy buildings in the tropics: A review. *Renewable and Sustainable Energy Reviews*, *186*, 113650. https://doi.org/10.1016/j.rser.2023.113650

[7] He, Z., Xie, W., Zhang, S., Gao, Y., Elnaggar, A. Y., Ren, J., El Azab, I. H., El-Bahy, Z. M., Yang, M., Zhang, H., & Guo, Z. (2024). Optimizing Spectral Properties of Cesium Tungsten Bronze Films Doped with Silver Nanowires Based on the Machine Learning Method. *The Journal of Physical Chemistry C*, *128*(38), 16093-16109. https://doi.org/10.1021/acs.jpcc.4c03634

[8] Kaspera, W., Wojas, J., Molenda, M., & Kotarba, A. (2016). Parallel migration of potassium and oxygen ions in hexagonal tungsten bronze – Bulk diffusion, surface segregation and desorption. *Solid State Ionics*, *297*, 1-6. https://doi.org/10.1016/j.ssi.2016.09.029

[9] Kim, M. S., Lee, H. K., Yoon, J. H., Kim, H. M., Kim, Y. S., & Kim, J. P. (2024). Improving dispersibility of tungsten oxide particles with organic ligands for photochromic films. *Colloids and Surfaces A: Physicochemical and Engineering Aspects*, *694*, 134083. https://doi.org/10.1016/j.colsurfa.2024.134083

[10] Kim, M. S., Yoon, J. H., Lee, H. K., Hirose, T., Takeda, Y., & Kim, J. P. (2024). Binder-enhanced reversible photochromic films by tungsten oxide hybrid composites for advanced applications. *Colloids and Surfaces A: Physicochemical and Engineering Aspects*, *703*, 135118.https://doi.org/10.1016/j.colsurfa.2024.135118

[11] Lee, J.-S., Liu, H.-C., Peng, G.-D., & Tseng, Y. (2017). Facile synthesis and structure characterization of hexagonal tungsten bronzes crystals. *Journal of Crystal Growth*, *465*, 27-33. https://doi.org/10.1016/j.jcrysgro.2017.02.044

[12] Li, P., Jiang, R., Zhao, L., Peng, H., Zhao, P., Jia, S., Zheng, H., & Wang, J. (2021). Cation Defect Mediated Phase Transition in Potassium Tungsten Bronze. *Inorg Chem*, *60*(23), 18199-18204. https://doi.org/10.1021/acs.inorgchem.1c02839

[13] Li, Q., Deng, S., Li, D., Yang, J., Jin, H., & Li, J. (2023). Tungsten bronze Cs_xWO_3 nanopowders doped by Ti to enhance transparent thermal insulation ability for energy saving. *Journal of Alloys and Compounds*, *944*, 169164. https://doi.org/10.1016/j.jallcom.2023.169164

[14] Liu, C., Peng, Y., Zhou, F., Yin, Y., Huang, X., Wang, L., Wang, W., Zhou, W., & Tang, D. (2018). Large-scale synthesis and quantitative characterization of size-controllable potassium tungsten bronze nanowires. *Journal of Physics D: Applied Physics*, *51*(9), 095305. https://doi.org/10.1088/1361-6463/aaa9dd

[15] Liu, J.-X., Shi, F., Dong, X.-L., Liu, S.-H., Fan, C.-Y., Yin, S., & Sato, T. (2015). Morphology and phase controlled synthesis of Cs_xWO_3 powders by solvothermal method and their optical properties. *Powder Technology*, *270*, 329-336. https://doi.org/10.1016/j.powtec.2014.10.032

[16] Liu, J., Ran, S., Fan, C., Qiao, Y., Shi, F., Yang, J., Chen, B., & Liu, S. (2019). One pot synthesis of Pt-doped Cs_xWO_3 with improved near infrared shielding for energy-saving film applications. *Solar Energy*, *178*, 17-24. https://doi.org/10.1016/j.solener.2018.12.007

[17] Machida, K., Wakabayashi, M., Ono, K., & Adachi, K. (2024). Oxygen vacancy-induced plasmonic and polaronic excitations in rubidium- and potassium-doped hexagonal tungsten bronzes. *Journal of Solid State Chemistry*, *332*, 124577. https://doi.org/10.1016/j.jssc.2024.124577

[18] Pathak, N., Pilania, R. K., Sooraj, K. P., Ranjan, M., Sarker, D., & Dube, C. L. (2025). Microwave-assisted rapid synthesis of non-stoichiometric tungsten oxide doped borosilicate glasses for NIR shielding application. *Ceramics International*, *51*(18), 24470-24480. https://doi.org/10.1016/j.ceramint.2025.03.130

[19] Ran, S., Liu, J., Shi, F., Fan, C., Chen, B., Zhang, H., Yu, L., & Liu, S.-H. (2018). Greatly improved heat-shielding performance of K_xWO_3 by trace Pt doping for energy-saving window glass applications. *Solar Energy Materials and Solar Cells*, *174*, 342-350. https://doi.org/10.1016/j.solmat.2017.08.013

[20] Shen, B., Wang, Y., Lu, L., & Yang, H. (2020). Synthesis and characterization of Sb-doped SnO_2 with high near-infrared shielding property for energy-efficient windows by a facile dual-titration co-precipitation method. *Ceramics International*, *46*(11), 18518-18525.https://doi.org/10.1016/j.ceramint.2020.04.157

[21] Shen, B., Wang, Y., Lu, L., & Yang, H. (2021). Spraying fabrication of spectrally selective coating with improved near-infrared shielding performance for energy-efficient glazing. *Ceramics International*, *47*(13), 18991-18997. https://doi.org/https://doi.org/10.1016/j.ceramint.2021.03.243

[22] Song, K., Weng, S., Zhou, J., Jiang, R., Cao, H., & Zhang, H. (2023). Tunable Optical Constants of Aluminum Tungsten Bronzes in Electrochromic Tungsten Oxide Thin Films. *The Journal of Physical Chemistry C*, *127*(36), 18036-18042.https://doi.org/10.1021/acs.jpcc.3c03521

[23] Song, X., Liu, J., Shi, F., Fan, C., Ran, S., Zhang, H., & Zou, Z. (2020). Facile fabrication of $K_mCs_nWO_3$ with greatly improved near-infrared shielding efficiency based on W^{5+}-induced small polaron and local surface plasmon resonance (LSPR) modulation. *Solar Energy Materials and Solar Cells*, *218*, 110769. https://doi.org/10.1016/j.solmat.2020.110769

[24] Suleiman, A. A., Parsi, A., Shakir, H. M., Rasouli, H. R., Pehlivanoğlu, D., & Kasırga, T. S. (2026). Synthesis of ultra-thin potassium tungsten bronze single crystals with optically contrasting domains and resistive switching. *Materials Today Nano*, *33*, 100735.https://doi.org/10.1016/j.mtnano.2025.100735

[25] Ta, N., Huang, J.-Y., He, S., Hanggai, W., & Chao, L.-M. (2024). Applications of optical control materials based on localized surface plasmon resonance effect in smart windows. *Tungsten*, *6*(4), 711-731. https://doi.org/10.1007/s42864-024-00273-1

[26] Wang, P., Liu, T., Zhao, S., Yang, Z., Ren, Z., Jiang, W., & Jiang, X. (2023). One-step ball-milling synthesis of cesium tungsten bronze nanoparticles and near-infrared shielding performance. *Ceramics International*, *49*(13), 21393-21401. https://doi.org/10.1016/j.ceramint.2023.03.268

[27] Wu, C.-M., Naseem, S., Chou, M.-H., Wang, J.-H., & Jian, Y.-Q. (2019). Recent Advances in Tungsten-Oxide-Based Materials and Their Applications. *Frontiers in Materials*, *6*, 49. https://doi.org/10.3389/fmats.2019.00049

[28] Wu, S., Wu, X., & Gao, Q. (2025). Modulation of NIR LSPR response via radial dopant inhomogeneity in tri-doped TiO_2 for energy-saving window. *Ceramics International*, *51*(1), 386-392. https://doi.org/10.1016/j.ceramint.2024.11.008

[29] Wu, X., Wang, J., Zhang, G., Katsumata, K.-i., Yanagisawa, K., Sato, T., & Yin, S. (2017). Series of M_xWO_3/ZnO (M = K, Rb, NH_4) nanocomposites: Combination of energy saving and environmental decontamination functions. *Applied Catalysis B: Environmental*, *201*, 128-136. https://doi.org/10.1016/j.apcatb.2016.08.030

[30] Yang, C., Chen, J. F., Zeng, X., Cheng, D., Huan, H., & Cao, D. (2016). Enhanced near-infrared shielding ability of (Li,K)-codoped WO_3 for smart windows: DFT prediction validated by experiment. *Nanotechnology*, *27*(7), 075203. https://doi.org/10.1088/0957-4484/27/7/075203

[31] Yang, G., Hu, D., Yang, C., Qi, Y., Liu, B., Chen, H., Zhang, L., Cui, Y., Yao, X., & Takats, V. (2021). Alkali metal tungsten bronze-doped energy-saving glasses for near-infrared shielding applications. *Ceramics International*, *47*(22), 31122-31129. https://doi.org/10.1016/j.ceramint.2021.07.286

[32] Yao, Y., Zhang, L., Chen, Z., Cao, C., Gao, Y., & Luo, H. (2018). Synthesis of Cs_xWO_3 nanoparticles and their NIR shielding properties. *Ceramics International*, *44*(12), 13469-13475. https://doi.org/10.1016/j.ceramint.2018.04.158

[33] Zhang, D., Liu, Y., & Tan, Y. (2026). Morphology-controlled synthesis of cesium tungsten bronze nanocrystals for enhanced NIR shielding performance. *Applied Surface Science*, *720*, 165270. https://doi.org/10.1016/j.apsusc.2025.165270

[34] Zhang, Y., Guo, D., & Li, R. (2022). Synthesis of $Cs_{0.3}WO_3$ with visible transparency and near-infrared absorption from commercial WO_3. *Journal of Solid State Chemistry*, *306*, 122768. https://doi.org/10.1016/j.jssc.2021.122768

[35] Zhao, J., & Du, Y. (2020). Multi-objective optimization design for windows and shading configuration considering energy consumption and thermal comfort: A case study for office building in different climatic regions of China. *Solar Energy*, *206*, 997-1017. https://doi.org/10.1016/j.solener.2020.05.090